

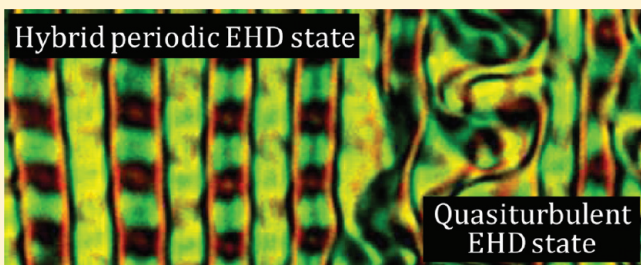
Competing Instability Modes in an Electrically Driven Bent-Core Nematic Liquid Crystal

Pramod Tadapatri and K. S. Krishnamurthy*

Centre for Soft Matter Research, P.O. Box 1329, Jalahalli, Bangalore 560013, India

 Supporting Information

ABSTRACT: Bent-core nematic electroconvection is a relatively less explored area, particularly in the low frequency regime. We focus here mainly on the instabilities occurring below 100 Hz in an initially planar monodomain of a bent-core nematic liquid crystal, which is negative in both conductivity and dielectric anisotropies. An unprecedented observation is the occurrence of three distinct bifurcation modes in a narrow region (10–17 Hz) that manifest, in the order of increasing threshold, as longitudinal, oblique and normal rolls. Whereas the second of these is the flexoelectrically enabled Carr–Helfrich mode, the other two are nonstandard electroconvection modes. Significantly, the first two instabilities remain unquenched even after bifurcation into the normal roll state below their respective codimension-2 points. The hybrid roll states display complex flows and morphologies. The study includes measurement of electrical parameters relevant to the discussion of results.



1. INTRODUCTION

Bent-core nematics (BCNs) have attracted much attention because of their many extraordinary properties not encountered in calamitic nematics (CNs). For instance, some BCNs have been found to show spontaneous formation of chiral domains of opposite handedness.¹ Similarly, there is ample evidence of short-range smectic order existing throughout the nematic range of bent-core compounds, even in the absence of an underlying smectic phase, unlike in most CNs.² Further, the anisotropic character of material properties differs for CNs and BCNs. For instance, the inequality between splay (k_{11}), twist (k_{22}), and bend (k_{33}) elastic moduli in calamitics is often expressible as $k_{33} > k_{11} > k_{22}$,³ whereas in BCNs it is found that $k_{11} > k_{33} > k_{22}$.^{4–7} Similarly, rotational viscosity (γ_1) is one order more for BCNs compared to CNs, and also the viscous relaxation appears to be a two-step process.^{4,5,8} In fact, in a recent discussion on the macroscopic and symmetry properties of nonpolar nematics composed of achiral molecules, the BCN phase is recognized as possibly possessing an octupolar or tetrahedratic order besides the usual quadrupolar order.⁹ While optically the tetrahedratic nematic may mimic the CN, it is capable of such extraordinary properties as are unobservable in the latter; for example, it may exist in ambidextrous helical ground states, exhibit Lehmann-like rotations, allow second harmonic generation, and respond anomalously to dielectric torques.

The uncommon behavior of BCNs extends also to electric field driven phenomena that form the subject of this paper. In some flexoelectric ("flexo", for brevity) experiments employing flexible electrodes, a BCN has been found to show giant values ($\sim nC\ m^{-1}$) for the bend flexocoefficient e_b .^{10–12} In other measurements using rigid electrodes, however, only

conventional e_b values ($\sim pC\ m^{-1}$) have been obtained.^{13,14} To resolve this discrepancy, a model of nonpolar molecular clusters showing quadrupolar flexoeffect has been advanced.¹⁴ However, energy conservation arguments seem to disallow giant values of flexomoduli;¹⁵ a radically new explanation of giant flexoeffect is based on monopole contribution in nematics confined between flexible electrodes and analogous to bilayer lipid membranes.¹⁶ As regards electroconvection (EC) in BCNs, since the initial experiments by Wiant et al.¹⁷ that highlighted its nonstandard aspects, there have been other studies^{5,18–20} revealing multiple scenarios of EC encompassing both standard and nonstandard features (see section 3.2 for details). In all these investigations, while the high frequency ($f = 10^2$ – 10^6 Hz) instabilities are elaborately studied, the effects due to static and low frequency fields are either not addressed or only briefly described. Thus we considered it worthwhile to closely examine the patterned states of the static and low frequency regimes in a BCN. While the effects observed in static fields are discussed in detail separately,²¹ here we focus on the competing modes of instability due to low frequency ($f = \omega/2\pi$) fields. We find three different interacting instability modes in the ac regime below 100 Hz, all of which are associated with cellular flows; we characterize the threshold and above threshold features of all these modes. The study also includes measurements on relevant electrical parameters.

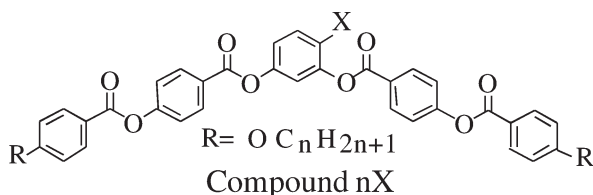
Received: October 28, 2011

Revised: December 12, 2011

Published: December 14, 2011

2. EXPERIMENTAL DETAILS

The material investigated, 4-chlororesorcinol bis[4-(4-*n*-undecanoyloxybenzoyloxy) benzoate] (**11Cl**), belongs to the series with the following chemical structure.



It was first synthesized by Weissflog et al.²² who employed optical, electro-optical, NMR, and X-ray methods to characterize the observed phases and reported the phase sequence of **11Cl** as

$$\text{Cr} \xrightarrow{\frac{88^\circ\text{C}}{[66]}} \left(\text{M} \xrightarrow{\frac{73^\circ\text{C}}{[8.6]}} \text{N} \xrightarrow{\frac{95^\circ\text{C}}{[0.6]}} \text{I} \right)$$

where Cr, N and I denote respectively the crystal, nematic and isotropic phases; the M phase, which is monotropically derived from the N, is optically isotropic and possesses a spontaneous chiral ordering as in a cholesteric blue phase; and the enthalpy changes within brackets are in kJ mol^{-1} . For the sample used in this study, the transition temperatures from optical microscopy were lower than the reported values by 2–3 °C, with the N–I transition temperature T_{NI} being 92 °C. We indicate the sample temperature T (K) by its reduced value $T^* = T/T_{\text{NI}}$.

The sample cells used for optical studies were sandwich type, constructed of indium tin oxide (ITO) coated glass plates. The planar alignment was secured by spin coating the ITO electrodes with polyimide and then buffering the coated surfaces unidirectionally on a tissue-paper. The rubbing direction and the layer normal define the reference axes x and z , respectively. Mylar spacers, heat-sealed to the electrodes through cooling from ~250 °C under a uniform pressure, determined the cell gap, which was measured interferometrically. For optical observations, a Carl Zeiss Axio Imager.M1m polarizing microscope equipped with an AxioCam MRc5 digital camera was used. The sample temperature T was maintained to an accuracy of ±0.1 °C by an Instec HCS402 hot-stage connected to a STC200 temperature controller. The voltage source was a Stanford Research Systems DS345 function generator coupled to a FLC Electronics voltage amplifier (model A800). Voltage was measured with a Keithley-200 multimeter. Specified voltage amplitudes of ac fields are the rms values, with the applied voltage $V(t) = \sqrt{2} V_{\text{rms}} \sin \omega t$. For dielectric and conductance spectra, a HP4194A Impedance/Gain-phase analyzer was used. The temperature variations of static permittivity $\epsilon(T)$ and conductivity $\sigma(T)$ at 1 kHz were determined using an Agilent 4284A precision LCR meter. In both dynamic and static measurements, the cell voltage was 0.5 V and the samples were magnetically aligned using a field $B \approx 1.38$ T from a Bruker B-MC1 electromagnet. As this B is several times the Fredericksz threshold corresponding to the d values used (~30 μm), we assume the easy axis or the initial director \mathbf{n}_0 to be along B . In these electrical measurements, the sample temperature was maintained by an Instec HS250 hot-stage connected to an RTC1 programmable temperature controller with an accuracy of 1 mK.

In the description of optical patterns, we indicate the setting of the polarizer P and analyzer A by P(α)–A(α'), where α and α'

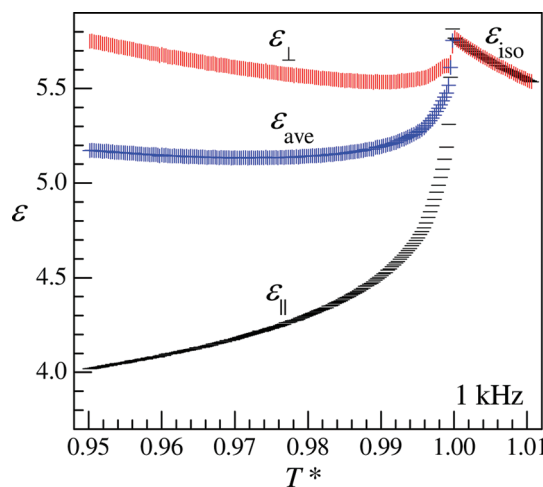


Figure 1. Temperature dependence of the principal components of static permittivity, $\epsilon_{||}$ and ϵ_{\perp} , in nematic **11Cl**, measured at 1 kHz. $\epsilon_{\text{ave}} = (\epsilon_{||} + 2\epsilon_{\perp})/3$; ϵ_{iso} is the permittivity in the isotropic phase.

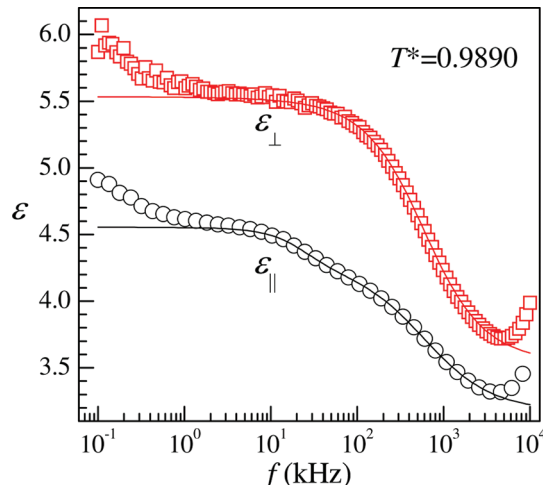


Figure 2. Frequency dependence of the real part of complex dielectric permittivity measured along and transverse to the nematic director at $T^* = 0.989$. The continuous lines are the fits to eq 1 in the text.

are angles (°) made by the corresponding transmission axes with the initial alignment direction x . For example, P(0)–A(90) signifies axially crossed polarizers, and P(45)–A(135), diagonally crossed polarizers. In specifying the electrical constraint in EC, we use the control parameter $\xi = (V/V_c)^2 - 1$, V_c denoting the critical voltage in general; V_W , V_L , and V_N denote the critical voltages of Williamslike oblique, longitudinal and inplane normal rolls, respectively. Similar notations are used in speaking of control parameters and critical wave numbers of different instabilities.

3. RESULTS AND DISCUSSION

3.1. Anisotropic Electrical Properties. The electrical properties of relevance to the field effects under study are the permittivity anisotropy $\epsilon_a = (\epsilon_{||} - \epsilon_{\perp})$ and conductivity anisotropy $\sigma_a = (\sigma_{||} - \sigma_{\perp})$, where the subscripts || and ⊥ refer to the directions relative to the nematic director. We have measured these quantities in the static and dynamic frequency regimes, at various

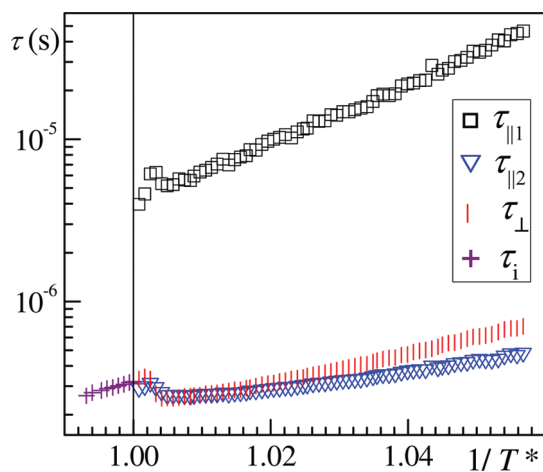


Figure 3. Temperature variation of dielectric relaxation times τ in the isotropic and nematic phases for the frequency range 100 Hz to 10 MHz; $\tau_{||1}$ and $\tau_{||2}$ correspond respectively to the Debye and Cole–Cole processes; τ_{\perp} and τ_i are for the Cole–Cole process governing the corresponding relaxations in the nematic and isotropic phases.

temperatures; the results of these measurements, useful for further discussions, are summarized below.

From the low-frequency $\varepsilon(T^*)$ data presented in Figure 1, it is seen that the static permittivity anisotropy in **11Cl** is negative in the entire nematic range. Further, the average permittivity $\varepsilon_{ave} = (\varepsilon_{||} + 2\varepsilon_{\perp})/3$ in the nematic phase increases toward the clearing point, with the line $\varepsilon_{ave}(T^*)$ leading discontinuously to the isotropic permittivity line $\varepsilon_{iso}(T^*)$. This is probably indicative of an antiparallel correlation between the longitudinal dipolar components of the neighboring molecules.²³ Representative data on the frequency dispersions $\varepsilon'(\omega)$ of the principal components of in-phase permittivity are given in Figure 2, for $T^*=0.989$ and frequency range 0.1 kHz to 10 MHz. $\varepsilon_{||}'(\omega)$ is characterized by two relaxation modes of which the lower frequency one is very weak; $\varepsilon_{||}'(\omega)$ shows a single strong relaxation at about the same frequency as that of the faster mode of $\varepsilon_{\perp}'(\omega)$. The dielectric response along \mathbf{n}_o is described by eq 1, where ε_s is the static permittivity, σ_s the static conductivity, ε_i the permittivity at the frequency limit of the i th mode, τ_i the relaxation time of the i th mode, and α the Cole–Cole distribution parameter; a and b are adjustable parameters. Equation 1 also describes $\varepsilon_{\perp}''(\omega)$, but with a single relaxation function of the Cole–Cole type. The fitted curves, shown by the continuous lines in Figure 2, are based on analyses of the data only up to 5 MHz. For higher frequencies, an artifact in the form of a rise in permittivity appears. This instrumental limitation renders τ_2 rather approximate.

$$\begin{aligned} \varepsilon^* = \varepsilon_2 &+ \frac{\varepsilon_s - \varepsilon_1}{1 + i\omega\tau_1} + \frac{\varepsilon_1 - \varepsilon_2}{1 + (i\omega\tau_2)^{1-\alpha}} - \frac{i\sigma_s}{\varepsilon_o\omega} \\ &+ \frac{a}{\omega^b} \end{aligned} \quad (1)$$

Evidently, the first of the longitudinal relaxations is a Debye like process; it is associated with the end-overend rotations of the molecules around their short axes, which are severely retarded by the nematic potential. On the other hand, both the longitudinal and transverse relaxations occurring around 0.5 MHz involve a Cole–Cole type mechanism; even in the isotropic phase, as seen

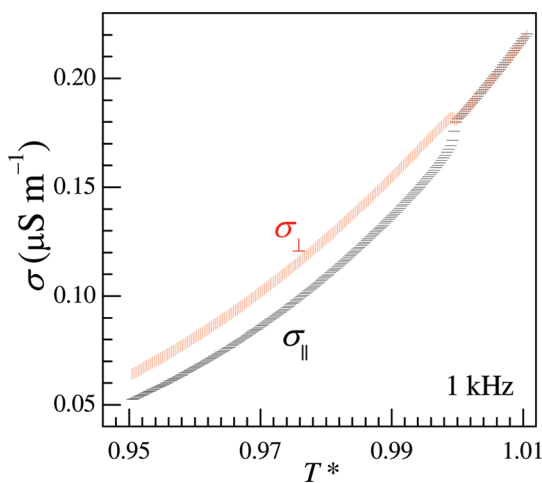


Figure 4. Temperature dependence of the principal components of static conductivity, $\sigma_{||}$ and σ_{\perp} , in nematic **11Cl**, measured at 1 kHz.

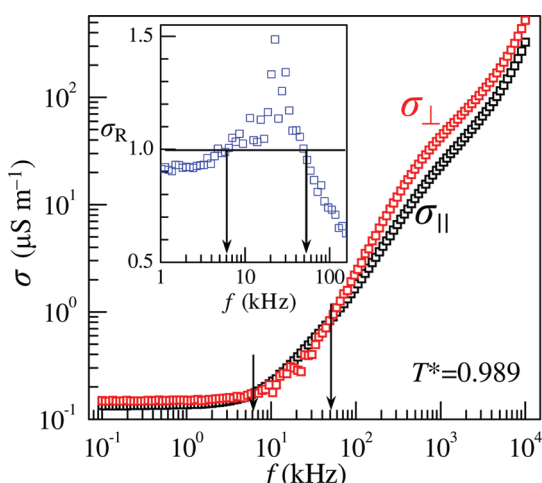


Figure 5. Frequency dependence of the principal electrical conductivities $\sigma_{||}$ and σ_{\perp} at $T^* = 0.989$ showing the σ_a sign reversals at about 6 and 50 kHz. Inset: The ratio $\sigma_R = \sigma_{||}/\sigma_{\perp}$ as a function of frequency in the dynamic region involving σ_a sign inversion points.

in Figure 3 depicting the temperature variation of relaxation times in the N and I phases, a similar relaxation is observed. These relaxations, characterized by a distribution of time constants, may arise due to independent rotations of dipolar groups around the long axis. In calamitics, the corresponding modes usually occur in the GHz region;²³ their large down shift here is ascribable to the increased molecular size and very high viscosity of the medium. Similar features of frequency variation of complex permittivity have previously been reported for the BCN compounds **12Cl**,²⁴ **9CN**,⁵ **12CN**,⁴ and **ClPbis10BB**.²⁵ In particular, from a comparison between the experimental and fitted curves $\varepsilon(\omega)$ for **ClPbis10BB**, it is inferred²⁵ that an additional relaxation exists in the high frequency region beyond 4 MHz for both the principal permittivities. Further, it is argued that, apart from molecular and intramolecular motions, collective modes are relevant for bent-core systems.

In Figure 4, we present temperature variation of the principal components of conductivity, $\sigma_{||}(T)$ and $\sigma_{\perp}(T)$, measured at

1 kHz and $T^* = 0.989$. Significantly, the static anisotropy σ_a is negative in the entire temperature range of the N phase; the ratio $\sigma_R = \sigma_{||}/\sigma_{\perp}$ increases almost steadily from ~ 0.82 near T_{MN} toward 1 as T_{NI} is approached. A similar σ_a behavior was also found very early for the static anisotropy in some calamitics such as 4,4'-diheptyloxyazobenzene (HOAB).²⁶ This departure from the usual σ_R value between 1 and 2 for most nematics is indicative of the slower ion diffusion along the director than across it; in other words, we may infer the presence of a short-range smecticlike layer order in the N phase. However, the N phase is macroscopically uniaxial. This is evident from our observation of the uniaxial figure in homeotropically aligned samples viewed conoscopically. It is relevant to note here that the X-ray patterns of oriented nematic 12Cl samples have shown the existence of cybotactic groups with the molecules tilted at 48° with respect to the layer normal; also, the M phase in 12Cl is found to be a layered phase, but with a reduced correlation length.²²

The frequency dependence of the principal conductivities, $\sigma_{||}(\omega)$ and $\sigma_{\perp}(\omega)$ shown in Figure 5 for $T^* = 0.989$ is typical of the dynamic conductivity features observed at various temperatures. The onset of conductivity relaxation is marked by a steep rise in σ occurring in the kHz region for both $\sigma_{||}$ and σ_{\perp} . While $\sigma_{||}$ begins to increase perceptibly at about 1 kHz, σ_{\perp} does so near 2 kHz; σ_a , which changes sign twice, first at about 6 kHz (f_1) and then near 50 kHz (f_2), is positive between these crossover points with σ_R reaching a maximum of ~ 1.5 (inset, Figure 5). While both f_1 and f_2 increase with temperature, the increase is marginal for f_1 compared to f_2 ; more specifically, between $T^* = 0.9562$ and $T^* = 0.9973$, f_1 shifts from 2.6 to 6 kHz, whereas f_2 shifts from about 8.7 to 90 kHz. The range f_{12} over which σ_a is positive scales exponentially with temperature according to f_{12} (kHz) = $3.936 + 8.432 \times 10^{-35} \exp(83.056 T^*)$.

3.2. Classical Flexoelectric and Electroconvective Patterned States. Before dealing with the experimental bifurcation scenarios in 11Cl, it is useful to dwell briefly on two of the established field induced effects which are of relevance to our later discussion. First of these is the Bobylev–Pikin (BP) effect which is a volume flexoelectric instability arising in layers with strong planar anchoring.²⁷ It involves a two-dimensional deformation characterized by the director deviation away from x , by an angle θ in the xz plane and φ in the xy plane. The director distribution is defined by $\theta = \theta_0 \cos(qy) \cos(\pi z/d)$ and $\varphi = \varphi_0 \sin(qy) \cos(\pi z/d)$, where d is the sample thickness and q , the angular wavenumber, is related to the spatial period of the pattern λ or the domain width w by $q = 2\pi/\lambda = \pi/w$. The threshold voltage V_F and wavenumber q_F of the BP flexoinstability are, under one elastic constant (k) approximation, given by²⁸

$$V_F = \frac{2\pi k}{|e^*|(1 + \mu)}, \quad \mu = \frac{\epsilon_0 \epsilon_a k}{e^{*2}} \quad (2)$$

$$q_F = \frac{2\pi}{\lambda_F} = \frac{\pi}{w_F} = \frac{\pi}{d} \sqrt{\frac{1 - \mu}{1 + \mu}} \quad (3)$$

where e^* denotes the difference in splay and bend flexoelectric moduli, $(e_s - e_b)$.

The second effect of interest here is the anisotropic EC which, in a nematic formed of rod-like molecules, is often driven by the Carr–Helfrich (CH) mechanism.^{27,29,30} For a planar sample with the initial director $\mathbf{n}_0 = (1, 0, 0)$, in a static field $\mathbf{E} = (0, 0, E)$, the one-dimensional CH analysis of the coupling between σ_a and the bend curvature distortion leads to formation of periodic space

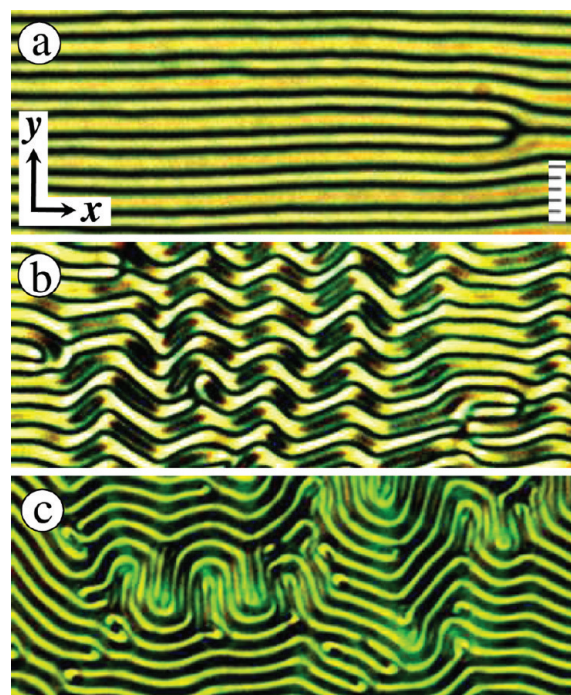


Figure 6. The Bobylev–Pikin flexoelectric instability excited by static fields in 11Cl at $T^* = 0.994$. (a) Domains formed along x as seen under nearly crossed polarizers P(0)–A(100), at $V = 1.43V_F$; the pattern involves periodic out-of-layer deviation θ and in-layer deviation φ of the director in bulk; the deviations decay from their maximum values in the $z = 0$ midplane to zero at the substrates. The alternation in color for successive bright bands correlates with alternation in the sign of φ . Along the near-extinction lines $\varphi = 0$. (b) Undulatory instability developed at $V = 1.79V_F$, seen between crossed polarizers P(0)–A(90). (c) Fingerprint texture at $V = 2.86V_F$ involving a chain of antiparallel topological dipoles; P(45).

charges of alternating sign along \mathbf{n}_o . The body force on these charges sets up periodic cellular flows above a critical voltage V_W determined by the balance between hydrodynamic, dielectric and elastic torques. The corresponding analysis for an ac field³¹ reveals the existence of a cutoff frequency f_c separating two regimes of instability: Below f_c , in the conduction regime, the space charges oscillate at the field frequency while the director pattern remains static; beyond f_c in the dielectric regime, the director and the velocities oscillate at the external frequency f , but the space charge polarity is nearly time independent. A three-dimensional generalization of the Carr–Helfrich theory, frequently referred to as the standard electroconvection (s-EC) model,^{32,33} captures many of the threshold features of anisotropic nematic EC such as the frequency dependence of the critical voltage V_W and wave vector $\mathbf{q}_W = (q_{Wx}, q_{Wy})$ of the roll pattern, and the spatiotemporal variation of the director, velocity and space charge fields.

The material parameters that play a crucial role in the Carr–Helfrich mechanism are σ_a and ϵ_a . Our understanding of anisotropic EC is essentially derived from experiments with uniaxial calamitic nematics having negative ϵ_a , positive σ_a , and planar initial alignment p ; this combination of electrical properties and director disposition, which we may conveniently refer to as the $(- + p)$ case, is established to be ideal for generating s-EC, which manifests optically as oblique rolls (ORs) with $(q_{Wx} \neq 0, q_{Wy} \neq 0)$, or as normal rolls (NRs) with $(q_{Wx} \neq 0, q_{Wy} = 0)$, the OR–NR transition taking place, under increasing f , at the triple or Lifshitz frequency $f_L < f_c$.³⁴ These standard rolls of the conduction regime,

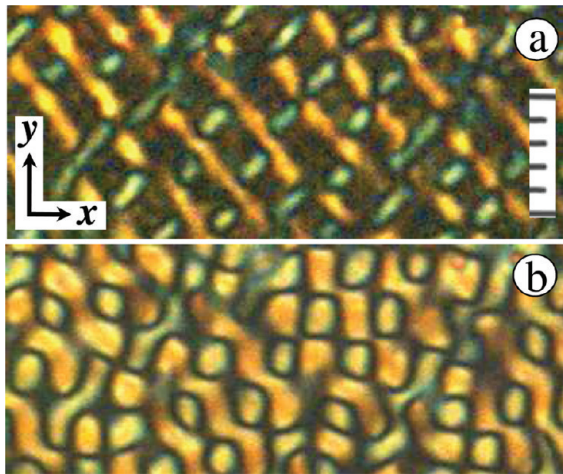


Figure 7. (a) Zig–zag domains involving opposite azimuthal deviations of the director and exhibiting different birefringence colors. (b) Same area as (a) after 1 s, showing growth of domains into a skewed varicose type morphology. Snapshots (a) and (b) are from time images recorded with 0.33 s frame-interval; brightness and contrast levels are doubled in (a) relative to (b); 0.1 Hz square wave field of voltage amplitude 2.5 V; nearly crossed polarizers P(0)–A(100); 4 μm scale division.

which are often referred to as Williams rolls (WRs), show a periodicity $\lambda \approx 1.5d$, d being the sample thickness. The dielectric rolls (DRs) that appear for $f > f_c$ are normal or oblique to \mathbf{n}_o depending on σ ,³⁵ their periodicity, which is independent of d but determined by the bend diffusion length, is usually much smaller than d . Further, even marginally above the threshold, they become unstable and give way to chevrons via defect chaos.^{36,37}

In recent years, there have been several studies on calamitics with other combinations of initial texture (planar, homeotropic or tilted), and signs of ϵ_a and σ_a .^{38–44} Thus, several electrohydrodynamic structures that do not conform to the standard model have come to light and they are often described as belonging to nonstandard EC (ns-EC).^{39,40} There have been some recent theoretical advances that incorporate flexoelectric effects in the standard model to account for some of the nonstandard features of EC.^{35,43,44}

By far, electric field generated patterned states in BCNs, as compared to CNs, have received only a limited attention.^{5,17–20,22,45–47} A brief survey of the experimental situation in this area is made in ref 19. Essentially, from the various studies on planar BC nematics, three distinct ns-EC states; one of them with a texture of broad bands along \mathbf{n}_o is what we call the inplane longitudinal roll (ILR) state; the other two, which are similar in their texture of broad bands normal to \mathbf{n}_o , are the inplane normal roll (INR) states; the INR2 state occurs prior to INR1, as f is increased; here “inplane” refers to the flow lines located in the layer plane. In their pioneering work on bent-core EC, Wiant et al.¹⁷ referred to the INR state as the prewavy (PW) state.

3.3. Patterned States Induced in 11Cl. In a static field, only the BP instability is excited. When the applied voltage is ~ 1.4 times the threshold $V_F = 2.8$ V, the (θ, φ) deformation bands appear between nearly crossed polarizers as in Figure 6a, with the wavevector predominantly along y . As expected for the BP instability or the variable grating mode (VGM), the frequency of these longitudinal domains increases in proportion to the applied field. Unlike in calamitics, the domains here are unstable

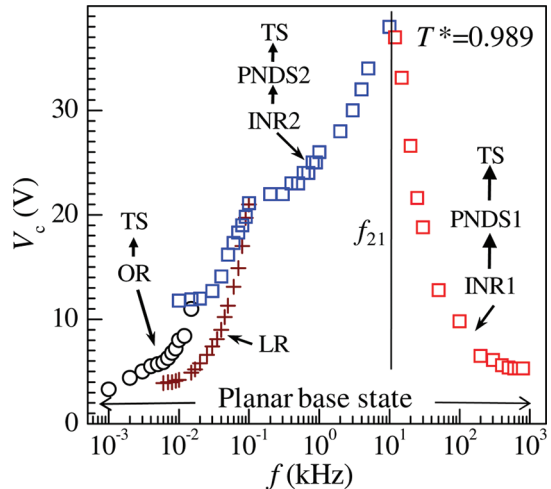


Figure 8. Critical voltage V_c for bifurcation into various patterned states as a function of frequency f at $T^* = 0.989$ in a 11Cl sample of thickness 5.5 μm . The data points cover the three main instability states corresponding to oblique rolls ORs, longitudinal rolls LRs, and inplane normal rolls INRs. Time-dependent state TS and propagating normal defect state PNDS are the above-threshold instabilities; f_{21} is the frequency of transition between the INR2 and INR1 states. Field applied was square wave up to 5 Hz and sinusoidal thereafter.

against long wavelength perturbations and become undulatory as in Figure 6b at $\sim 1.8 V_F$. Far away from threshold, π -disclinations of opposite topological charge develop within the domain structure and the wavevector direction changes with location as in a cholesteric fingerprint texture (Figure 6c). The above threshold transformations of the domain structure that eventually lead to a morphological situation as in layered systems are described in detail elsewhere.²¹

In the ac regime, several complex effects occur. Under a quasi-static square wave field of low frequency (0.001–0.02 Hz), well above the dc threshold, the VGM is excited during field constancy; for example, we observed the domains at ~ 4 V for 1 mHz. The pattern decays during every polarity reversal and reforms on the field becoming steady. Between 0.02 and 0.4 Hz, flexoeffect couples with EC resulting in crosslike domains²¹ and oblique rolls (Figure 7). Above 0.4 Hz, interestingly, the BP instability is completely absent and only EC effects are observed. We have made a systematic study of the patterned states occurring above 1 Hz. We present the phase diagram of 11Cl in Figure 8, showing the frequency dependence of critical voltage at which the various instabilities optically manifest. The instabilities occurring over a wide range of f (1 Hz to 1 MHz) constitute six distinct regimes involving four different primary bifurcations: Region I from about 1–6 Hz in which only the OR state is formed; region II (~ 6 –9 Hz) involves two EC states, LR and OR; in region III (~ 10 –17 Hz) LR, OR and INR2 states occur in the order of increasing threshold. Region IV that follows extends up to ~ 100 Hz; here, within the initial LR state, INR2 sets in as a secondary instability. Beyond 100 Hz and up to 10 kHz (region V), only the INR2 state is found; likewise, the high frequency regime from 10 to 10^3 kHz (region VI) belongs exclusively to the INR1 state.

In region I, the rest state transforms into a periodic Williams-like EC state at a well-defined critical voltage $V_c = V_w$. The resulting optical texture observable by shadowgraphic imaging is illustrated in Figure 9. Figure 9a shows one of the snapshots

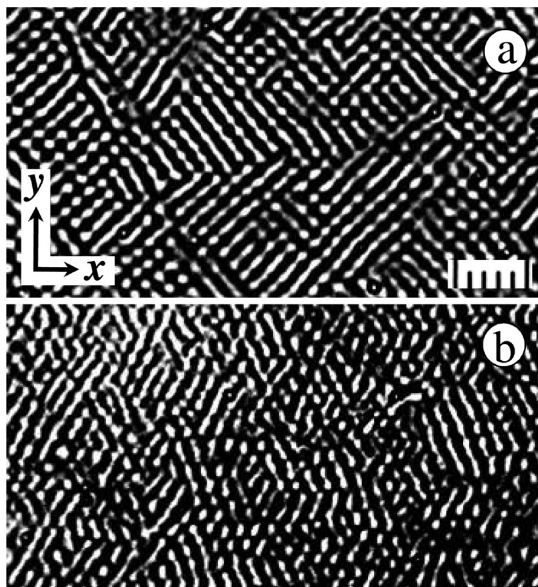


Figure 9. Williamslike oblique rolls formed in the low frequency region under square wave driving, P(45). (a) 1 Hz, 3.3 V, (b) 4 Hz, 5.3 V; 4 μm scale division.

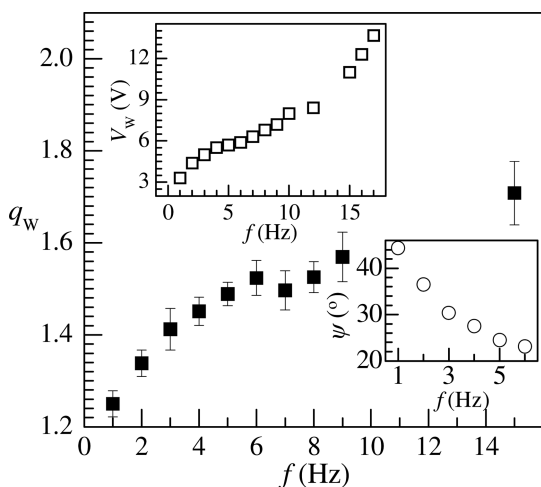


Figure 10. Threshold characteristics of Williamslike oblique rolls observed between 1 and 17 Hz. q_w is the critical wavenumber in π/d units; V_W is the critical voltage from the data in Figure 8 replotted on a linear frequency scale; ψ is the critical roll-inclination angle relative to y .

from a time series, recorded using a square wave field (1 Hz, 3.3 V) and a single polarizer P(45); the oblique rolls here have a periodicity of $\sim 2d$. The images of the series were of varied optical contrasts and the texture shown is the one with maximum visibility. The time dependence of contrast is only to be expected. When the period of ac is large, voltage induced diffuse counterion layers tend to form next to the electrodes; this would modify the field so that it is lower in bulk, and rapidly increasing toward the electrodes in the Debye-like screening layers.⁴⁸ The charging process following a polarity reversal in itself may occupy a very short time, less than a millisecond. But the time for charge drift t_d across the cell may be much longer. For example, from $t_d = d^2/(vV)$ with v as the mobility ($\sim 10^{-11} \text{ m}^2 \text{ V}^{-1} \text{ s}^{-1}$), for a 5.5 μm thick sample subject to 3.3 V, t_d is about 0.9 s. At 1 Hz,

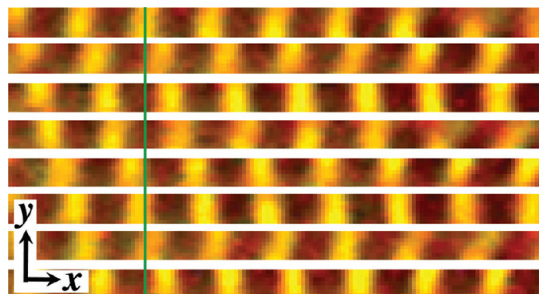


Figure 11. Snapshots of drifting near normal rolls obtained at $T^* = 0.989$, $f = 15 \text{ Hz}$ and $\xi_W = 0.3$; P(45); interval between successive frames is 0.14 s. Separation of adjacent bright bands is $\sim 3.7 \mu\text{m}$. Drift frequency $\sim 1.2 \text{ Hz}$.

therefore, between polarity reversals, the bulk field is unsteady and lower than that corresponding to the applied voltage. Soon after polarity switchover, while the double layers reform, the potential in bulk increases. This explains the time variation of distortion amplitude. The bimodal texture in Figure 9a probably corresponds to a voltage slightly above threshold. The measurement of true threshold at low frequencies is rendered somewhat inaccurate by the dynamics of electrode polarization, which may be further complicated by selective adsorption of ions at aligning layers and differential mobility of opposite charge carriers.⁴⁹

In region I, the inclination of the ORs to the y -axis, ψ , reduces drastically with increase in f . This is evident from a comparison of the rolls in Figures 9a,b. As further depicted in the bottom inset in Figure 10, ψ drops from $\sim 45^\circ$ at 1 Hz to $\sim 22^\circ$ at 6 Hz. The critical voltage V_W for the OR state, as seen in the top inset of Figure 10, increases nonlinearly with f , tending toward saturation in region I, but showing a trend change in regions II and III where it increases more and more rapidly. The critical wavenumber as a function of frequency $q_w(f)$ shows a similar trend (Figure 10), but the increase in q_w beyond region I is much less pronounced. These quantitative results on threshold parameters will be discussed later.

An important property of the ORs in **11Cl** is their temporally coherent oscillations observed above threshold in region I (see the video clip “oscillatory rolls” in the Supporting Information, SI). Such an oscillatory instability has been known for long in calamitics.^{50,51} At higher frequencies, these rolls exhibit the propagative phenomenon or Hopf bifurcation, as depicted in the time images in Figure 11 for 15 Hz, $\xi_W = 0.3$ (see the video clip “traveling rolls” in the SI). Traveling rolls are well-known in s-EC observed with $(-+)$ nematics and is explained by the weak electrolyte model based on electrodiffusion involving two ionic species.⁵² The first observation of Hopf bifurcation in the $(--)$ case was in a calamitic.⁴¹

Between 6 and 100 Hz, in region II–IV of the phase diagram (Figure 8), the primary bifurcation from the structureless field-free state into a periodic patterned state occurs at a critical field. This bifurcation is of the forward type in that the transition is reversible without hysteresis. The optical pattern is one of longitudinal rolls (LRs) or stripes stretching predominantly along the easy axis \mathbf{n}_o . At threshold $E_L = V_L/d$, it appears localized to some areas and becomes extended with field elevation. This aspect is generally traceable to surface irregularities causing minute variations in the threshold for different regions. It may arise from mechanical rubbing of the polyimide coating that produces grooves of varying dimensions along x ; it may also be

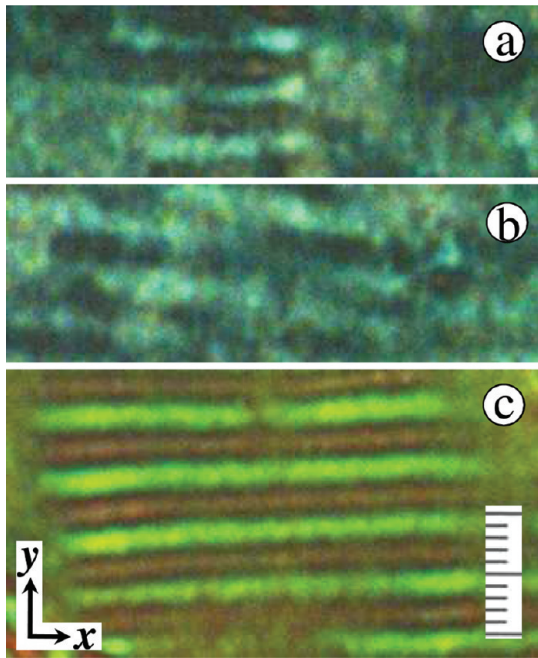


Figure 12. Longitudinal rolls at $T^* = 0.989, f = 40$ Hz. (a, b) Threshold ($\xi_L \approx 0$) texture of LRs exhibiting poor contrast and localized formation; in (a), the domains are along x or the initial director n_o ; in (b), they are at a slight angle to x . (c) LRs well above threshold ($\xi_L = 1.4$); the green and dull-brown bands correspond to regions with opposite azimuthal tilts. The period of the pattern is about $9.5 \mu\text{m}$; $2 \mu\text{m}$ scale division. $d = 5.5 \mu\text{m}$.

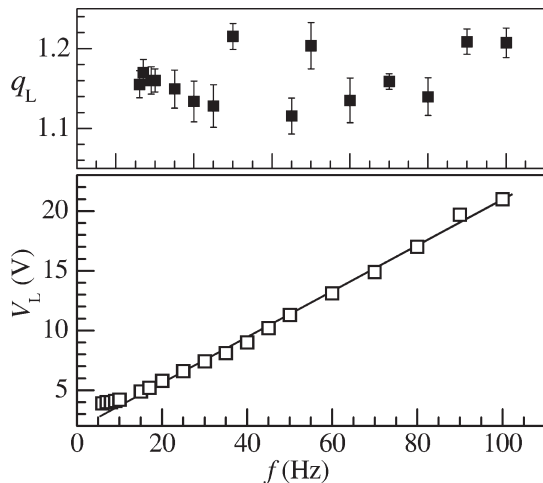


Figure 13. Threshold characteristics of longitudinal rolls observed between 6 and 100 Hz. q_L is the critical wavenumber in π/d units; V_L is the critical voltage from the data in Figure 8 replotted on a linear frequency scale.

due to impurities at the substrates that disturb the alignment. An important characteristic of LRs is that they are not visualizable by shadowgraphic imaging. In other words, unlike ORs which act as an array of cylindrical lenses for the extraordinary component of polarized light along n_o and produce focal lines transverse to n_o ,²⁹ LRs do not corrugate a planar extraordinary wavefront passing through the layer. Thus, near onset, the director modulation corresponding to LRs does not involve an out-of-plane tilt periodicity; rather the periodicity is that of azimuthal deviation,

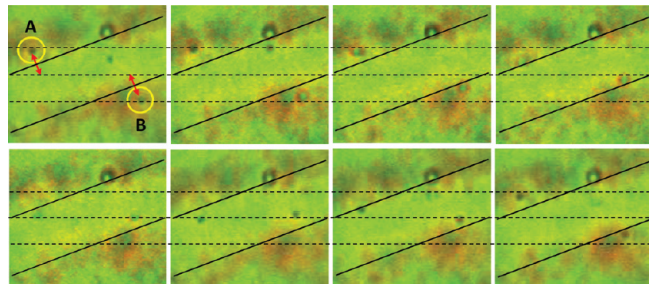


Figure 14. Time series of the longitudinal domain pattern demonstrating cellular flows through motion of dust particles. 1.2 s between successive frames. Nearly diagonal, crossed polarizers. The particles A and B are at the centers of yellow circles in the first frame. Oblique black lines are axes of flow. Dashed lines indicate the limits between which the particles circulate, appearing to oscillate along red arrows. Dark and bright images of the particles correspond to their location below and above the midplane, respectively.

which reveals itself under birefringence contrast. In Figure 12, we see LRs in partially crossed polarizers $P(0)$ – $A(100)$. From Figure 12a,b showing the threshold textures, it is clear that the wavevector of the localized domains is either along y or at a slight angle to it. Well above threshold, as in Figure 12c, the alternation of interference colors for successive bright bands corresponding to alternating signs of φ becomes clearly discernible. However, the optical contrast between the dark and bright regions of the LR texture remains generally poor because of the absence of light focusing unlike for the classical WRs. Again, as the control parameter ξ_L is increased, unlike in s-EC where a regular sequence of ordered stationary states follow the primary bifurcation well before ξ reaches 1.5,⁵³ the LR structure exhibits a remarkable stability against secondary instabilities over a wide range of ξ_L . For instance, in Figure 12c, $\xi_L \approx 1.4$, yet the domains retain their threshold geometry and no long wavelength perturbations as in varicose structure are noticeable. Even in respect of frequency variation of critical voltage V_L and wavenumber q_L , the LR instability possesses unusual features. While V_L is linear in f , q_L is nearly independent of f . This is demonstrated in Figure 13, where the $V_L(f)$ data of Figure 6 are replotted on a linear f -scale; and $q_L(f)$ data are from the same localized domain region as used for critical voltage measurements. By contrast, in s-EC, $V_W(f)$ diverges at the cutoff frequency of the conduction regime f_c , and $q_W(f)$ is a smooth curve of ever increasing slope.

The LR instability is hydrodynamic. This is demonstrated by the time series of the oblique LR pattern in Figure 14. Here, the nature of cellular flows associated with the domains is revealed by the motion of dust particles. The particles A and B are at the centers of yellow circles in the first frame. Oblique black lines represent the axes of flow. Dashed lines indicate the limits between which the particles circulate, appearing to oscillate along red arrows. Dark and bright images of the particles correspond to their location below and above the midplane, respectively. The period of circulation is about 7.5 s.

The aforementioned characteristics of LRs in **11Cl** are all very similar to those observed by Katona et al.⁴¹ in the (–) calamitic compound 4-n-octyloxy-phenyl-4-heptyloxy-benzoate (**8/7**). They describe the threshold as a field threshold rather than a voltage threshold as in the case of DRs. Although we have not made a detailed study of $V_L(d)$, we have found the critical voltage for a $12.1 \mu\text{m}$ thick layer to be nearly twice that for

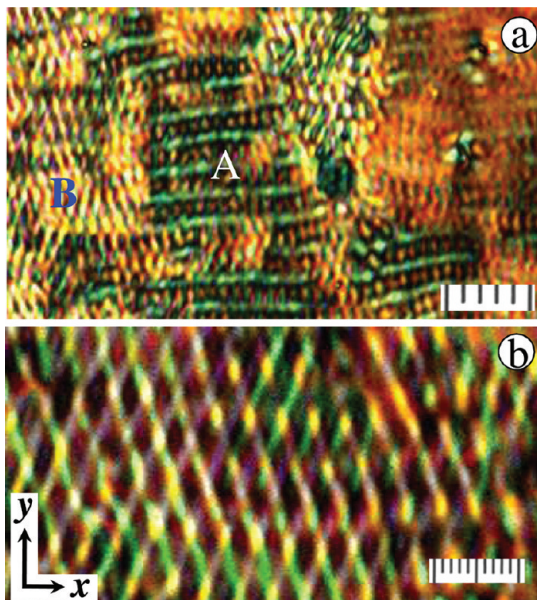


Figure 15. Coexistence of ORs and LRs at the critical voltage for the onset of the OR state. (a) LRs and ORs are dominant respectively in regions A and B. (b) An enlarged OR region showing a rhombic lattice of focal points: 12 Hz, 8.9 V, $T^* = 0.989$, partially crossed polarizers P(0)–A(100). Scale division: 5 μm in (a) and 1 μm in (b).

a 5.5 μm thick layer to which Figure 8 applies. The significant new aspect of our study concerns the crossover of the LR state to the Williamslike OR state described above. Figure 15a shows a typical texture observed at the crossover voltage of about 8.9 V, at 12 Hz. The near normal zigzag stripes in region B are due to EC explicable by the extended CH theory.^{43,44} The horizontal blue-green bands in region A are LRs. Notably, the LR state is not quenched soon after the onset of the OR. It persists even after the appearance of INRs. The coexistence of LR, OR and INR states at the threshold of INR2 is shown in Figure 16. In Figure 16a, while ORs show up dominantly below the indicated diagonal, INRs are prominent above the diagonal. Periodic interference color changes occur both along and across the ORs, as better seen in the enlargement in Figure 16b. The color variations arise from (θ, φ) modulations along x as well as y . The coupling between the OR and INR modes is reflected in the period of the former, which is drastically reduced from $\sim 1.5d$ before the onset of INR state (Figure 15) to $\sim 0.55d$ now. The existence of LRs, together with ORs and INRs well above their thresholds, is seen in Figure 16c, which depicts a texture at 15 Hz, and 14.6 V corresponding to $\xi_L = 7.5$, $\xi_w = 0.76$ and $\xi_N = 0.48$. This situation is reminiscent of the coexistence of flexodomains and EC rolls in a hybrid aligned film of MBBA exposed to a static field.⁵⁴

In region IV of the phase diagram, the interacting LR and INR2 modes often result in complex pattern modifications. At 40 Hz, for example, LRs appear as in Figure 17a when $\xi_L = 0.78$; the INR texture is already seen near the top left corner where the threshold seems lowered due to alignment disturbance. In Figure 17b, a hybrid LR-INR pattern is formed just above the INR2 threshold; periodicity of the pattern along both x and y in localized columnar regions implies a 2-dimensional modulation in these regions. On raising ξ_N to 0.15 (Figure 17c), besides the occurrence of increased distortion and strong light focusing effects in patterned columns along y , remarkably, there is near

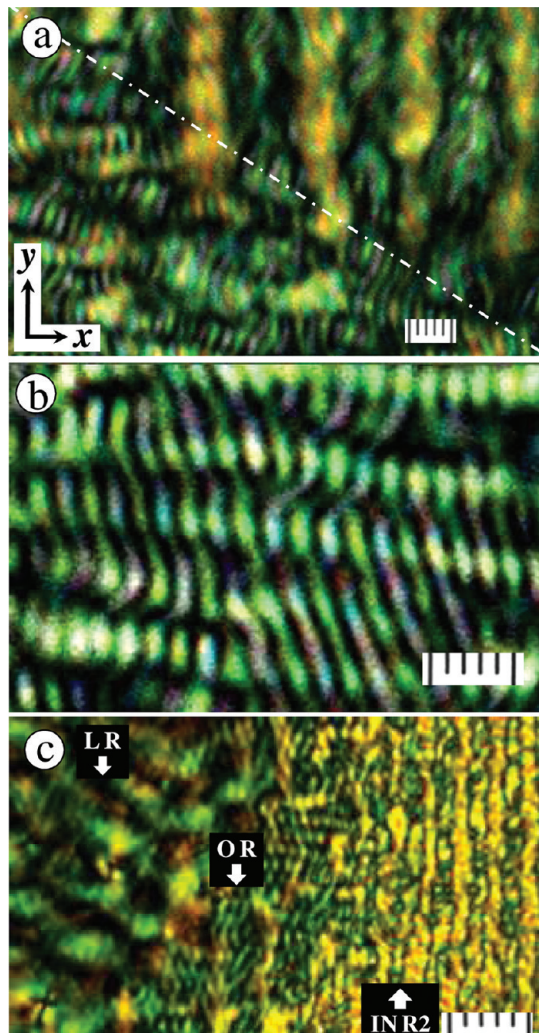


Figure 16. Coexistence of LR, OR and INR states at the threshold of INR2. (a) ORs and INRs are dominant respectively below and above the white diagonal. (b) An enlarged OR region showing periodic color changes both along and across the domains. The color variations arise from (θ, φ) modulations along x as well as y . Due to the coupling between the OR and INR modes, the period of the former is drastically reduced from $\sim 1.5d$ before the onset of INR state to $\sim 0.55d$ now. The horizontal dark bands in the region of ORs in (a, b) are due to the LR state not quenched completely. (c) LR, OR and INR2 states formed in succession; 15 Hz, 14.6 V, $T^* = 0.989$, partially crossed polarizers P(0)–A(100); scale division: 1 μm in (a, b), 4 μm in (c).

absence of modulation in the intervening bands between these columns. At $\xi_N = 0.3$, we obtain a quasiturbulent situation (Figure 17d). At a lower frequency (30 Hz), unpatterned bands appear less conspicuous (Figure 18a) and spectacular flows are observed within the patterned columns. In each of these columns, such as indicated by the rectangular box in Figure 18a, pairs of birefringent “beads” appear periodically along y . The beads exhibit time varying pattern of colors and extinction brushes; a careful examination of the changing birefringence of beads reveals rotation of the fluid taking place about y ; the rotation is opposite for an adjacent (along x) pair of beads, and is in the same sense for any column of beads; these facts are readily ascertained in the time series pictures in Figure 18b–e (see also the video clip “vortices” in the SI). As is well established,^{5,17–20}

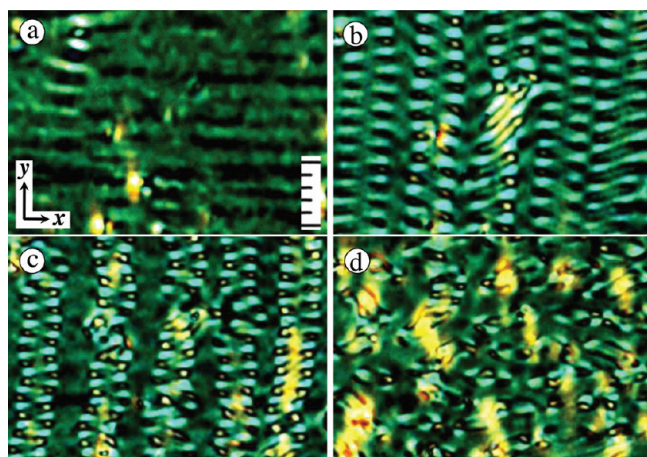


Figure 17. Bifurcation of the LR state into the INR2 state. (a) LRs at 12 V (control parameter for LRs, $\xi_L = 0.78$); the INR texture is already seen near the top left corner where the threshold seems lowered due to alignment disturbance. (b) Coexistence of LR and INR states just above the INR2 threshold; periodicity of the pattern along both x and y in localized columnar regions implies a 2-dimensional modulation in these regions. (c) Continued coexistence of the two states when INR2 control parameter ξ_N is raised to 0.15; increased distortion is seen in strong light focusing effects; in the intervening bands between patterned columns, remarkably, modulation is almost absent. (d) Quasiturbulent state at $\xi_N = 0.3$.

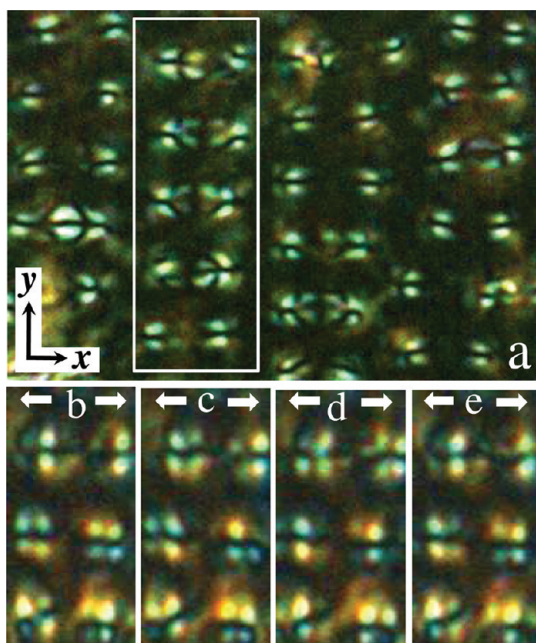


Figure 18. (a) Hybrid LR-INR2 texture at 30 Hz, 14 V ($\xi_N = 0.22$), under crossed polarizers P(0)–A(90), exhibiting columns of paired, birefringent “beads”, such as enclosed by the rectangular box. The birefringence pattern at the beads changes with time repetitively. (b–e) Time series of the pattern of beads with ~ 0.3 s between successive snapshots. The white arrows indicate the sense of fluid rotation revealed by the changing extinction brushes and birefringence colors of beads; 16 V ($\xi_N = 0.59$).

in the INR state, the plane of the vortices coincides with the layer plane and the rotation axis is z . By contrast, in the LR state, the

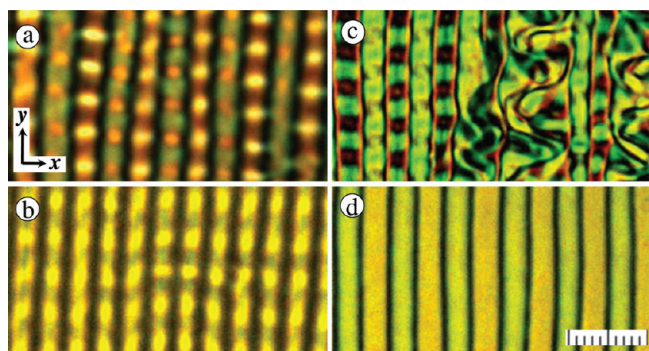


Figure 19. (a–c) Hybrid LR-INR2 texture at 80 Hz. (a) Columns of birefringent “beads” for partially crossed polarizers P(0)–A(105); $\xi_N = 0.22$; streamlines are in the layer plane as indicated by motion of foreign particles along the dark bands between columns of beads; the particles move mainly along $\pm y$, with the directions for adjacent tracks being opposite. (b) Same as (a) but for a single polarizer P(0), showing the beads as focal images mainly due to periodic out-of-plane director tilts both along x and y . (c) Quasiturbulent state extending from right to left at $\xi_N = 3.7$; partially crossed polarizers, P(45)–A(0). (d) The texture of INRs at 500 Hz; $\xi_N = 2.4$; P(0)–A(105). 2 μm scale division.

flows occur largely about x . It seems, therefore, rather intricate to find the cellular flows in the hybrid state of LR and INR taking place about y . When the frequency in region IV is increased sufficiently, the flow field changes to that of the INR2 state, and the birefringent beads appear steady as in Figure 19a. That the beads are essentially the focal images due to periodic out-of-plane director deviations along both x and y is shown by the texture in Figure 19b recorded with a single polarizer along \mathbf{n}_o . The hybrid state persists well above ξ_{N_0} , even into the state of temporal disorder (Figure 19c). In the absence of any coupling with other modes, the INR2 morphology consists merely of wide periodic stripes, as in Figure 19d for 500 Hz. The INR2 and INR1 instabilities, which involve similar (θ, φ) modulations and show identical morphologies, are characterized elaborately in various earlier reports.^{5,17–20} We reconfirm here that their occurrence has no direct correlation with the sign of electrical anisotropies. The INR2 exists from 10 Hz to 10 kHz; while ε_a remains negative throughout this range, σ_a reverses sign at ~ 6 kHz, being negative below the isotropy point. The INR2 bifurcation line shows a discontinuity at the codimensional-2 (C2) point where it meets the threshold line of the LR state (Figure 8); the increase in the threshold of INR2 with f is rapid and slightly nonlinear below this point as compared to the slow linear rise above it. The INR1 occurs in both $(-+)$ and $(--)$ situations with continuously decreasing threshold for increasing f .

3.4. Significance of the Patterned States Observed in 11CI. We may first consider the possible reasons for the absence of ORs in dc, particularly in view of the excitation of these rolls in ac. In the $(--)$ case, the CH mechanism breaks down regardless of the field being static or alternating. However, inclusion of flexoterms in the s-EC model reactivates it. The volume torque $\boldsymbol{\Gamma}$ from the coupling of dipolar flexopolarization with the applied field in the presence of director gradient involves $(e_s - e_b)$, and that from quadrupole density with the field gradient, $(e_s + e_b)$. In dc, the bulk field is likely to be homogeneous and hence the gradient flexotorque $\boldsymbol{\Gamma}_G = -(e_s + e_b) \mathbf{n} \times \nabla E$ would be zero. On the other hand, in ac, consequent on polarity change, the field gradients that come to exist in bulk may generate a nonzero $\boldsymbol{\Gamma}_G$ as

long as $(e_s + e_b) \neq 0$. If the sign of Γ_G is such as to destabilize the planar state and support the CH process, bifurcation to the periodic EC state could occur. Another factor to consider concerns time scales: In thin samples, the director relaxation may not be sufficiently slow in relation to charge relaxation for the conductive instability to be sustainable. That this is not the case in **11Cl** becomes evident when we evaluate the director and charge relaxation times τ_d and τ_q . For a rough estimate, we may use the expressions applicable to the unpatterned state: $\tau_d = \gamma_1 d^2 / k_{11} \pi^2$ and $\tau_q = \epsilon_o \epsilon_{\perp} / \sigma_{\perp}$. At $T^* = 0.989$, from the data in Figures 1 and 3, $\tau_q \approx 0.32$ ms; from the collapse rate of Brochard-Leger wall for **11Cl** discussed in ref 21, $\gamma_1 / k_{11} \approx 0.34$ s μm^{-2} , so that, for $d = 5.5$ μm , $\tau_d \approx 1$ s is about three orders above τ_q . Finally, charge injection present under static and quasistatic fields due to imperfections in the aligning layer may exercise a disrupting influence on the CH charge focusing process. This may be sufficient to suppress the roll instability especially when conductivity anisotropy responsible for charge focusing is weak, as in the case of **11Cl**.⁵⁵

We may also consider the absence of flexodomains in ac above ~ 1 Hz. Recently, it has been shown⁵⁶ that, under ac excitation, flexodomain solutions of dielectric and conduction symmetries exist for all q_F between 0 and ∞ . For a given elastic anisotropy $k_a = (k_{11} - k_{22}) / (k_{11} + k_{22})$ and e^* , the threshold for either symmetry increases with frequency and could easily exceed the EC threshold even at 1 Hz that corresponds here to $\omega \tau_d \approx 6.3$ (see Figure 7 in ref 56).

All the competing instability modes described above arise in the $(- -)$ situation, far below the frequency region in which permittivity and conductivity relaxations occur (Figures 2 and 5). The standard model of electroconvection does not provide for any instability in this case. According to this model,³² for a planar monodomain and $f < f_c$, the threshold voltage V_o appropriate to the wave vector $\mathbf{q} = (q_x, q_y)$ is given by the dispersion relation

$$V_o^2 = \frac{\pi^2 k^*}{\epsilon_o \epsilon_a^* - \frac{\sigma_a^* \tau_q \alpha_2}{\eta^*}}, \quad \text{with } \tau_q = \frac{\epsilon_o \epsilon_{\perp}}{\sigma_{\perp}} \quad (4)$$

Here $(*)$ signifies the effective value of the corresponding material parameter, explained in ref 32 and 33; η^* denotes the effective viscosity, α_2 , one of the Leslie viscosity coefficients and τ_q , the charge relaxation time. While all the starred quantities involve the components of \mathbf{q} , the electrical anisotropies depend additionally on the field frequency. From eq 4, it is readily seen that, to have a real threshold, $(\epsilon_o \epsilon_a^* - \sigma_a^* \tau_q \alpha_2 / \eta^*) > 0$. The coefficient α_2 , from entropic considerations, is required to be negative, and measurements are in accord with this condition. In the present case, calculations using the measured electrical parameters show $\epsilon_o \epsilon_a^* \approx -9.2$ pF m $^{-1}$ and $\sigma_a^* \tau_q \approx +4.7$ pF m $^{-1}$; from previous measurements, it may generally be assumed that $|\alpha_2 / \eta^*| < 1$; thus, the condition for real V_o fails, and yet we realize experimentally the OR state, which is Williamslike in its periodic θ -distortion. In fact, EC in the $(- - \text{p})$ situation was first studied by Goscianski and Leger;^{57,58} they conjectured the zigzag domains, predominantly directed along \mathbf{n}_o , to arise from an amplification of twist fluctuations caused by the positive Leslie coefficient α_3 . Since then there have been several observations of similar instabilities which are interpreted differently as due to pretilt conditions,⁵⁹ isotropic electrolytic mechanism involving charge density gradients along the field,^{38,60} and the coupling between CH and flexoelectric mechanisms.^{43,44,61,62} Subsequent

theoretical extensions of the one-dimensional⁶³ and three-dimensional^{64,65} CH models that took flexopolarization $P_F = \epsilon_s \mathbf{n}(\nabla \cdot \mathbf{n}) + e_b(\mathbf{n} \cdot \nabla) \mathbf{n}$ into account underscored the importance of flexoeffect to the occurrence of EC in the $(- - \text{p})$ case. In recent years, significant advances have been made in the analysis of both flexoeffect and EC based on the extended SM.^{43,44,56} For example, the predictions on threshold parameters are discussed in ref 43 for low frequencies $\omega' = \omega \tau_q$ from near 0 to 3; we may compare these with our results for ORs occurring in the very limited ω' range 0.012 to 0.034 (Figure 10). The variation $V_W(\omega')$ predicted using the material parameters of 4-methoxybenzylidene-4-n-butylaniline (MBBA), except for $e^* = 7.97$ pC m $^{-1}$ and $\sigma_R = 0.8$, is one of smooth increase, at a progressively decreasing rate; the predicted curve for $\sigma_R = 1$ showing the same trend lies lower (see Figure 14 in ref 56). We observe in **11Cl** with $\sigma_R \approx 0.9$ the same trend in the beginning; but the curve slopes upward with increase in ω' (upper inset, Figure 10), which may indicate a smaller e^* (see Figure 12a in ref 56). Regarding the critical wavenumber, the analytical curve $q_W(\omega')$ for $e^* = 7.97$ pC m $^{-1}$ is also a smoothly increasing one (Figure 12b, in ref 56); we observe a similar dependence in Figure 10. Likewise, for the same e^* , away from $\omega' = 0$, the inclination of rolls ψ is expected to be a rapidly decreasing function of ω' (Figure 12c, in ref 56). This trend is also seen in Figure 10 (lower inset). We may add that $e^* = 7.97$ pC m $^{-1}$ used in ref 56 is nearly the same as our calculated value for **11Cl** in ref 21.

The longitudinal stripes morphology may be obtained in different situations as comprehensively surveyed previously.^{66–68} In dc or very low frequency ac, as a nonhydrodynamic (θ, φ) modulated instability, with the wavenumber scaling as the field, it is driven by the Bobylev-Pikin mechanism. The LR instability, on the other hand, is hydrodynamic, observed in ac over a relatively large frequency range, associated with a field independent period, and without significant θ -modulation. It has some similarity with the Pikin–Indenbom (PI) azimuthal CH instability²⁷ arising in tilted nematics and involving periodic rotation of the director about x or z . The large initial tilt required for a low threshold as obtained here is ordinarily not conceivable in a sample bound between buffed polyimide coatings. However, as recently emphasized,⁶⁹ the presence of supramolecular smectic C clusters in the N phase may involve a large tilt favoring inlayer fluctuations; this could promote the PI instability. A further facilitating factor is this: As shown by Derzhanski and Petrov for the dc case⁷⁰ the PI threshold reduces substantially when the gradient flexoterm is included in the torque balance equation. We may, therefore, tentatively consider the LR mode as the gradient flexoelectrically modified PI instability. In any case, the LR mode is to be treated differently from the OR mode governed by the extended CH mechanism. The LR instability is completely quenched beyond the C2 point where the LR bifurcation line meets the INR2 line. Similarly, the OR instability persists only until the corresponding C2 point. This situation is reminiscent of the competition between Freedericksz and EC modes in $(++)$ nematics with a small positive ϵ_s , where EC with a lower threshold below the C2 point is predicted to disappear beyond the C2 frequency.⁷¹

We may also note that the LR state differs from the PW state of CNs. For example, the PW instability observed by Huh et al.⁷² in the bend Freedericksz state of a $(- +)$ compound is characterized by (i) linear frequency variation of threshold voltage, (ii) near f -independence of critical period, (iii) critical period in the range $4d$ – $6d$ and (iv) flow field involving flows along and

across the domains, in addition to a roll-rotation type flow. While the LR state observed in the (—) case of 11Cl and the PW state may appear similar in respect of characteristics (i) and (ii), they differ regarding (iii) and (iv). Further, the PW domains run perpendicular to the plane of director tilt in the Freedericksz state; by contrast, the LRs form broadly along the easy axis.

Finally, localized hybrid instabilities as in Figure 16 demonstrate the extreme morphological sensitivity to excitation conditions involving changes in material properties. This has been pointed out previously by Brand et al.,⁷³ who observed pattern localization due to a change in the sign of α_3 in a (—) compound.

4. CONCLUSIONS

Our studies on the BCN 11Cl have shown the existence of three different competing and coexisting instability modes with varying symmetries in the low frequency region. The coexistence is observed to involve linear superpositions as well as nonlinear modifications, depending on the driving conditions. Interestingly, all the instabilities are electroconvective and appear for the same (—) combination of electrical anisotropies. The threshold features of the OR instability broadly agree with the flexoelectrically enabled s-EC model.⁵⁶ That the OR state is distinctly different from the LR is significant; it implies that the two EC instabilities are actually governed by different parameters. While, like ORs, LRs may perhaps be interpreted as due the extended CH effect, the extension now involves, besides field inhomogeneity, weak azimuthal anchoring and initial director tilt, so that gradient flexo-enabled PI destabilization may become effective. The LR instability may arise from the extended PI effect that takes field inhomogeneity into account. The INR2 mode is presently to be classified as of ns-EC category. The LR and INR2 modes possess contrasting characteristics: Their wavevectors lie in orthogonal directions in the layer plane, along \mathbf{n}_o for INRs and transverse to it for LRs; their flow vortices occur in orthogonal planes, in xy planes for INRs and yz planes for LRs; while LRs maintain constant spatial frequency under increasing control parameter, INRs constitute a voltage varying grating; while the threshold of the LR state scales linearly with field, that of the other is nonlinear and discontinuous. The coupling of these modes produces some spectacular effects like columns of birefringent ‘beads’ that occur in counter rotating pairs at relatively lower frequencies, and a two-dimensional network of steady focal images with inplane flows at higher frequencies. The interplay and coexistence of these modes well into the quasiturbulent state is a challenging nonlinear, nonequilibrium phenomenon in electroconvection.

■ ASSOCIATED CONTENT

S Supporting Information. Three video clips of electrically excited patterns in the bent-core nematic liquid crystal 11Cl at $T^* = 0.989$: (a) “oscillatory rolls” at 6 Hz for crossed polarizers and control parameter $\xi_W = 0.28$; (b) “traveling rolls” at 15 Hz for a single polarizer at 45° to the easy axis and $\xi_W = 0.3$; and (c) “vortices” of flow in the coupled LR-INR2 mode at 30 Hz, for $\xi_N = 0.22$ and crossed polarizers. The birefringence patterns in the bead-like localized regions exhibit spatiotemporal variations that reveal rotation of the fluid about the vertical direction; the rotation is opposite for an adjacent pair of beads along a row, and is in the same sense for any column of beads. This material is available free of charge via the Internet at <http://pubs.acs.org>.

■ AUTHOR INFORMATION

Corresponding Author

*Phone: +91 80 28381119. Fax: +91 80 28382044. E-mail: murthyksk@gmail.com.

■ ACKNOWLEDGMENT

We thank Prof. K. A. Suresh and Dr. Praveer Asthana for the experimental facilities. We are indebted to Prof. W. Weissflog for the bent-core compound used in this study.

■ REFERENCES

- (1) Tamba, M. G.; Baumeister, U.; Pelzl, G.; Weissflog, W. *Liq. Cryst.* **2010**, *37*, 853–874 and refs 39 and 40 therein.
- (2) Tschierske, C.; Photinos, D. J. *J. Mater. Chem.* **2010**, *20*, 4263–4294.
- (3) Pasechnik, S. V.; Chigrinov, V. G.; Shmeliova, D. V. *Liquid Crystals: Viscous and Elastic Properties*; Wiley-VCH: Weinheim, Germany, 2009.
- (4) Tadapatri, P.; Hiremath, U. S.; Yelamaggad, C. V.; Krishnamurthy, K. S. *J. Phys. Chem. B* **2010**, *114*, 1745–1750.
- (5) Tadapatri, P.; Krishnamurthy, K. S.; Weissflog, W. *Phys. Rev. E: Stat., Nonlinear, Soft Matter Phys.* **2010**, *82*, 031706(15).
- (6) Sathyaranayana, P.; Mathew, M.; Li, Q.; Sastry, V. S. S.; Kundu, B.; Le, K. V.; Takezoe, H.; Dhara, S. *Phys. Rev. E: Stat., Nonlinear, Soft Matter Phys.* **2010**, *81*, 010707(4)(R).
- (7) Majumdar, M.; Salamon, P.; Jákli, A.; Gleeson, J. T.; Sprunt, S. *Phys. Rev. E: Stat., Nonlinear, Soft Matter Phys.* **2011**, *83*, 031701(8).
- (8) Dorjgotov, E.; Fodor-Csorba, K.; Gleeson, J. T.; Sprunt, S.; Jákli, A. *Liq. Cryst.* **2008**, *35*, 149–155.
- (9) Brand, H. R.; Pleiner, H. *Eur. Phys. J. E* **2010**, *31*, 37–50.
- (10) Harden, J.; Mbanga, B.; Éber, N.; Fodor-Csorba, K.; Sprunt, S.; Gleeson, J. T.; Jákli, A. *Phys. Rev. Lett.* **2006**, *97*, 157802(4).
- (11) Harden, J.; Teeling, R.; Gleeson, J. T.; Sprunt, S.; Jákli, A. *Phys. Rev. E: Stat., Nonlinear, Soft Matter Phys.* **2008**, *78*, 031702(5).
- (12) Jákli, A. *Liq. Cryst.* **2010**, *37*, 825–837.
- (13) Le, K. V.; Araoka, F.; Fodor-Csorba, K.; Ishikawa, K.; Takezoe, H. *Liq. Cryst.* **2009**, *6*, 1119–1124.
- (14) Kumar, P.; Marinov, Y. G.; Hinov, H. P.; Hiremath, U. S.; Yelamaggad, C. V.; Krishnamurthy, K. S.; Petrov, A. G. *J. Phys. Chem. B* **2009**, *113*, 9168–9174.
- (15) Castels, F.; Morris, S. M.; Coles, H. J. *AIP Adv.* **2011**, *1*, 032120(4).
- (16) Petrov, A. G. Private Communication.
- (17) Wiant, D.; Gleeson, J. T.; Éber, N.; Fodor-Csorba, K.; Jákli, A.; Tóth-Katona, T. *Phys. Rev. E: Stat., Nonlinear, Soft Matter Phys.* **2005**, *72*, 041712(12).
- (18) Tanaka, S.; Dhara, S.; Sadashiva, B. K.; Shimbo, Y.; Takanishi, Y.; Araoka, F.; Ishikawa, K.; Takezoe, H. *Phys. Rev. E: Stat., Nonlinear, Soft Matter Phys.* **2008**, *77*, 041708(5).
- (19) Tadapatri, P.; Hiremath, U. S.; Yelamaggad, C. V.; Krishnamurthy, K. S. *J. Phys. Chem. B* **2010**, *114*, 10–21.
- (20) Kaur, S.; Belaissaoui, A.; Goodby, J. W.; Gortz, V.; Gleeson, H. F. *Phys. Rev. E: Stat., Nonlinear, Soft Matter Phys.* **2011**, *83*, 041704(12).
- (21) Tadapatri, P.; Krishnamurthy, K. S.; Weissflog, W. *Soft Matter* DOI: 10.1039/c1sm06870a.
- (22) Weissflog, W.; Sokolowski, S.; Dehne, H.; Das, B.; Grande, S.; Schroder, M. W.; Eremin, A.; Diele, S.; Pelzl, G.; Kresse, H. *Liq. Cryst.* **2004**, *31*, 923–933.
- (23) Chandrasekhar, S. *Liquid Crystals*; Cambridge University Press: Cambridge, England, 1992.
- (24) Pelzl, G.; Eremin, A.; Diele, S.; Kresse, H.; Weissflog, W. *J. Mat. Chem.* **2002**, *12*, 2591–2593.
- (25) Salamon, P.; Éber, N.; Buka, Á.; Gleeson, J. T.; Sprunt, S.; Jákli, A. *Phys. Rev. E: Stat., Nonlinear, Soft Matter Phys.* **2010**, *81*, 031711(11).

- (26) Rondelez, F. *Solid State Commun.* **1972**, *11*, 1675–1678.
- (27) Pikin, S. A. *Structural Transformations in Liquid Crystals*; Gordon and Breach Science Publishers: New York, 1991.
- (28) Bobylev, Y. P.; Pikin, S. A. *Sov. Phys. JETP* **1977**, *45*, 195–198.
- (29) Blinov, L. M.; Chigrinov, V. G. *Electrooptic Effects in Liquid Crystal Materials*; Springer: Berlin, 1994.
- (30) Helfrich, W. *J. Chem. Phys.* **1969**, *51*, 4092–4105.
- (31) Dubois-Violette, E.; de Gennes, P. G.; Parodi, J. *J. Phys. (Paris)* **1971**, *32*, 305–317.
- (32) Bodenschatz, E.; Zimmermann, W.; Kramer, L. *J. Phys. (Paris)* **1988**, *49*, 1875–1899.
- (33) Kramer, L.; Pesch, W. In *Pattern Formation in Liquid Crystals*; Buka, Á., Kramer, L., Eds.; Springer: Berlin, 1996.
- (34) Ribotta, R.; Joets, A.; Lei, L. *Phys. Rev. Lett.* **1986**, *56*, 1595–1597.
- (35) May, M.; Schopf, W.; Rehberg, I.; Krekhov, A.; Buka, Á. *Phys. Rev. E: Stat., Nonlinear, Soft Matter Phys.* **2008**, *78*, 046215(9).
- (36) Rossberg, A. G.; Kramer, L. *Physica D* **1998**, *115*, 19–28.
- (37) Scheuring, M.; Kramer, L.; Peinke, J. *Phys. Rev. E: Stat., Nonlinear, Soft Matter Phys.* **1998**, *58*, 2018–2026.
- (38) Kochowska, E.; Nemeth, S.; Pelzl, G.; Buka, Á. *Phys. Rev. E: Stat., Nonlinear, Soft Matter Phys.* **2004**, *70*, 011711(9).
- (39) Buka, Á.; Éber, N.; Pesch, W.; Kramer, L. In *Self Assembly, Pattern Formation and Growth Phenomenon in Nano-Systems*; Golovin, A. A., Nepomnyashchy, A. A., Eds.; Springer: Berlin, 2006.
- (40) Buka, Á.; Éber, N.; Pesch, W.; Kramer, L. *Phys. Rep.* **2007**, *448*, 115–132.
- (41) Tóth-Katona, T.; Cauquil-Vergnes, A.; Éber, N.; Buka, Á. *Phys. Rev. E: Stat., Nonlinear, Soft Matter Phys.* **2007**, *75*, 066210(12).
- (42) Kumar, P.; Patil, S. N.; U. S. Hiremath, U. S.; Krishnamurthy, K. S. *J. Phys. Chem. B* **2007**, *111*, 8792–8800.
- (43) Krekhov, A.; Pesch, W.; Éber, N.; Tóth-Katona, T.; Buka, Á. *Phys. Rev. E: Stat., Nonlinear, Soft Matter Phys.* **2008**, *77*, 021705(11).
- (44) Tóth-Katona, T.; Éber, N.; Buka, Á.; Krekhov, A. *Phys. Rev. E: Stat., Nonlinear, Soft Matter Phys.* **2008**, *78*, 036306(12).
- (45) Heuer, J.; Stannarius, R.; Tamba, M. G.; Weissflog, W. *Phys. Rev. E: Stat., Nonlinear, Soft Matter Phys.* **2008**, *77*, 056206(11).
- (46) Kovalenko, L.; Schroder, M. W.; Reddy, R. A.; Diele, S.; Pelzl, G.; Weissflog, W. *Liq. Cryst.* **2005**, *32*, 857–865.
- (47) Tanaka, S.; Takezoe, H.; Éber, N.; Fodor-Csorba, K.; Vajda, A.; Buka, Á. *Phys. Rev. E: Stat., Nonlinear, Soft Matter Phys.* **2009**, *80*, 021702(8).
- (48) Barbero, G.; Olivero, D.; Scaramuzza, N.; Strangi, G.; Versace, C. *Phys. Rev. E: Stat., Nonlinear, Soft Matter Phys.* **2004**, *69*, 021713(8).
- (49) Thurston, R. N.; Cheng, J.; Meyer, R. B.; Boyd, G. D. *J. Appl. Phys.* **1984**, *56*, 263–272.
- (50) Krishnamurthy, K. S. *Jpn. J. Appl. Phys.* **1984**, *23*, 1165–1168.
- (51) Hirata, S.; Tako, T. *Jpn. J. Appl. Phys.* **1983**, *22*, 1073–1079.
- (52) Treiber, M.; Kramer, L. *Mol. Cryst. Liq. Cryst.* **1995**, *261*, 311–326.
- (53) Ribotta, R. In *Solitons in Liquid Crystals*; Lam, L., Prost, J., Eds.; Springer: Berlin, 1992.
- (54) Delev, V. A.; Krekhov, A. P.; Kramer, L. *Mol. Cryst. Liq. Cryst.* **2001**, *366*, 849–856.
- (55) Krishnamurthy, K. S.; Kumar, P. *Phys. Rev. E: Stat., Nonlinear, Soft Matter Phys.* **2007**, *76*, 051705(8).
- (56) Krekhov, A.; Pesch, W.; Buka, Á. *Phys. Rev. E: Stat., Nonlinear, Soft Matter Phys.* **2011**, *83*, 051706(13).
- (57) Goscianski, M. *Philips Res. Rep.* **1975**, *30*, 37–55.
- (58) Goscianski, M.; Leger, L. *J. Phys. (Paris)* **1975**, *36*, C1–231–235.
- (59) Tikhomirova, N. A.; Ginzberg, A. V.; Kirsanov, E. A.; Bobyshev, Yu. P.; Pikin, S. A.; Adomenas, P. V. *JETP Lett.* **1977**, *24*, 269–272.
- (60) Blinov, L. M.; Barnik, M. I.; Lazareva, V. T.; Trufanov, A. N. *J. Phys. (Paris)* **1979**, *40*, C3–263–268.
- (61) Kai, S.; Hirakawa, K. *Solid State Commun.* **1976**, *18*, 1573–1577.
- (62) Petrescu, P.; Giurgea, M. *Phys. Lett. A* **1976**, *59*, 41–42.
- (63) Madhusudana, N. V.; Raghunathan, V. A. *Liq. Cryst.* **1989**, *5*, 1789–1812.
- (64) Thom, W.; Zimmermann, W.; Kramer, L. *Liq. Cryst.* **1989**, *4*, 309–316.
- (65) Kramer, L.; Bodenschatz, E.; Pesch, W.; Thom, W.; Zimmermann, W. *Liq. Cryst.* **1989**, *5*, 699–715.
- (66) Hinov, H. P.; Vistin, L. K. *J. Phys. (Paris)* **1979**, *40*, 269–292.
- (67) Hinov, H. P.; Bivas, I.; Mitov, M. D.; Shoumarov, K. *Liq. Cryst.* **2003**, *30*, 945–959.
- (68) Hinov, H. P.; Bivas, I.; Mitov, M. D.; Shoumarov, K.; Marinov, Y. *Liq. Cryst.* **2003**, *30*, 1293–1317.
- (69) Petrov, M.; Keskinova, E.; Katranchev, B.; Naradikian, H. *Liq. Cryst.* **2011**, *38*, 41–52.
- (70) Derzhanski, A.; Petrov, A. G. In *Advances in Liquid Crystal Research and Applications*; Bata, L., Ed.; Pergamon Press: Oxford, 1980; pp 515–521.
- (71) Dressel, B.; Pesch, W. *Phys. Rev. E: Stat., Nonlinear, Soft Matter Phys.* **2003**, *67*, 031707(7).
- (72) Huh, J.-H.; Yusuf, Y.; Hidaka, Y.; Kai, S. *Phys. Rev. E: Stat., Nonlinear, Soft Matter Phys.* **2002**, *66*, 031705(6).
- (73) Brand, H. R.; Fradin, C.; Finn, P. L.; Pesch, W.; Cladis, P. E. *Phys. Lett. A* **1998**, *235*, 508–514.